Numerical investigation of Western current intensification in wind-driven ocean model

In the context of Computational Fluid Dynamics Project supervised by A.Venaille

CONTENTS

1 Introduction 1

2 Theoretical Background 1
- I Munk-Stommel Model . . . 1
  - A Nonlinear Formulation 1
  - B Adimensionalization . 2
- II Steady-State Study 2
  - A Linear System Study 2
  - B Non-linear system study 3
  - C Inertial layer study . 4

3 Numerical implementation 4
- I finite difference formulation . 4
  - A Jacobian formulation 4
  - B Friction stability . . . 5
  - C CFL-like considerations 5

4 Results & Discussion 5
- I Boundary layer 5
- II Dynamics 6
  - A Rossby solutions . . 6
  - B Low non-linear regime 9
  - C High non-linear regime 9
- III Wind stress distribution . . . 10

5 Conclusion 10

INTRODUCTION

Western boundary currents, such as the Gulf Stream in the North Atlantic and the Kuroshio in the North Pacific, are among the most striking large-scale features of the world's oceans. These narrow, swift currents channel immense quantities of heat, salt, and momentum, making them crucial drivers of both regional and global ocean circulation. Their pronounced intensification along the western boundaries of ocean basins, a phenomenon known as western intensification, has attracted considerable attention since the mid-twentieth century.

The foundational theoretical explanations for western intensification are often traced to the seminal works of Stommel (1948) and Munk (1950). In Stommel's model, the essential balance is established among the β-effect (latitudinal variation of the Coriolis parameter), an idealized wind stress forcing, and a linear frictional term. By including the β-effect in a simple, rectangular ocean basin, Stommel demonstrated how a poleward intensification of the boundary current necessarily emerged on the western side. Stommel's treatment introduced the concept of a "Stommel boundary layer," where frictional and β-related effects interact to create a narrow, intensified current region.

Shortly thereafter, Munk (1950) proposed an alternative view in which viscous dissipation (parameterized through eddy viscosity) is the dominant frictional mechanism, rather than linear drag. Despite the contrasting frictional closures (linear in Stommel's model versus harmonic viscosity in Munk's), both models capture the essential physics that leads to boundary current intensification on the western edges of subtropical gyres.

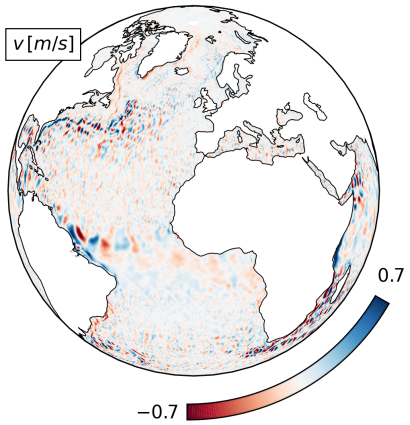

Figure 1.1 – Atlantic Ocean surface meridional velocity (v), the western intensification near west coastlines is clearly visible with the main GulfStream structure.

Contemporary understanding embraces these complications and recognizes that the intensification process is not merely a simple interplay of β-induced Rossby waves and linear friction but also involves robust mesoscale eddy activity, inertial effects, and large-scale atmospheric variability. Current high-resolution observations and numerical simulations confirm the persistent role of the western boundary in concentrating kinetic energy and heat transport, underscoring the remarkable predictive power of Stommel's and Munk's theoretical underpinnings.

THEORETICAL BACKGROUND

Munk, in 1950, proposed a model for western boundary current intensification in the ocean, neglecting the nonlinear terms in the full development. This assumption was made considering that nonlinear terms primarily affect the symmetry of the solutions and do not significantly alter the global behavior of western intensification. He successfully derived western intensification with this simplified approach but was unable to explain northern intensification and the transient processes generally observed.

I. Munk-Stommel Model

A. Nonlinear Formulation

To derive the Munk-Stommel model, we will use a homogeneous ocean model governed by shallow water equations. Many other approaches can be used (e.g., vertical integration of the planetary geostrophic equations for Boussinesq fluids or quasi-geostrophic formulation), but these are beyond the scope of this study. In this context, the potential vorticity is expressed as:

$$\frac{D}{Dt}\left(\frac{f+\zeta}{h}\right) = \frac{F}{h} \tag{2.1}$$

where f is the Coriolis parameter, and F is the curl of the stresses applied to the fluid. Under the beta-plane approximation:

$$f = f_0 + \beta y$$

and considering a flat bottom and a rigid lid (with $\frac{Dh}{Dt}$ negligible over horizontal variations), we introduce Ψ, the stream function, satisfying:

$$v = \partial_x \Psi,\ u = -\partial_y \Psi,\ \zeta = \Delta \Psi$$

Thus, using the Jacobian $\mathcal{J}(\Psi, \zeta)$ as the advective derivative, we obtain:

$$\frac{\partial \zeta}{\partial t} + \mathcal{J}(\Psi, \zeta) + \beta \frac{\partial \Psi}{\partial x} = F \tag{2.2}$$

Next, we focus on deriving the F term. In this model, stresses are assumed to act only at the top and bottom of the ocean. The bottom limitation represents the main thermocline boundary (Munk), which must be considered when modeling specific phenomena.

At the top, the stress is expressed as wind stress (τ_x, τ_y), which is assumed to be a known function in this study. At the bottom, various approaches can be used: in the Stommel approach, stress is considered a linear function of velocity, while in the Munk approach, it is modeled as harmonic viscosity. Here, we consider a combination of both:

$$F = \nabla \times \boldsymbol{\tau} - r\Delta\Psi + A\Delta\zeta \tag{2.3}$$

This results in the following formulation of the model:

$$\frac{\partial\zeta}{\partial t}+\mathcal{J}(\Psi,\zeta)+\beta\frac{\partial\Psi}{\partial x} = \nabla\times\boldsymbol{\tau}-r\Delta\Psi+A\Delta\zeta \tag{2.4}$$

B. Adimensionalization

To minimize the number of parameters, we introduce the following scaling (Carrier and Robinson):

$$\hat{t} \to \beta L t, \quad \hat{x} \to \frac{x}{L}, \ \hat{\Psi} \to \frac{\beta}{|\tau|}\Psi$$

where $|\tau|$ is the mean magnitude of the rotational wind stress. This scaling is derived from the consideration of a "Sverdrupian" leading balance (Wallis), i.e., the equilibrium between the Coriolis force and the wind stress in the basin's interior, where nonlinear terms can be neglected (to be discussed further), resulting in steady states. Under this rescaling, the leading-order terms in the interior basin are of unity order:

$$\beta\frac{\partial x}{\partial\Psi} \sim \nabla \times_z \boldsymbol{\tau}$$

Using this scaling, we rewrite (2.4), omitting the hats, as:

$$\begin{aligned}\frac{\partial\zeta}{\partial t}+\mathcal{R}\mathcal{J}(\Psi,\zeta)+\frac{\partial\Psi}{\partial x}\\ = \nabla \times_z \boldsymbol{\tau} - \epsilon_{\mathcal{S}}\Delta\Psi + \epsilon_{\mathcal{M}}\Delta\zeta\end{aligned} \tag{2.5}$$

where the parameters are defined as:

$$\mathcal{R} = \frac{|\tau|}{\beta^2 L^3}, \quad \epsilon_{\mathcal{S}} = \frac{r}{\beta L}, \quad \epsilon_{\mathcal{M}} = \frac{A}{\beta L^3}$$

If L is comparable to the Earth's radius, $\mathcal{R}$ represents the Rossby number for this problem, with the Sverdrupian velocity $U = \frac{|\tau|}{\beta L^2}$. The Reynolds number can then be expressed as $Re = \frac{UL}{A}$. In the viscous boundary layer, the speed scaling is expected to follow $Re = \frac{\mathcal{V}\delta}{A}$, where δ is the width of the viscous layer.

II. Steady-State Study

As previously mentioned, for relatively low Rossby numbers (on the order of ...), a steady state can be expected, consistent with the Sverdrupian balance. This state satisfies the following relation:

$$\begin{aligned}\mathcal{J}(\Psi,\zeta) + \frac{\partial\Psi}{\partial x} = \nabla \times_z \boldsymbol{\tau}\\ - \epsilon_{\mathcal{S}}\Delta\Psi + \epsilon_{\mathcal{M}}\Delta\zeta\end{aligned} \tag{2.6}$$

A. Linear System Study

In the case of a small Rossby number, the advection term can be neglected, and the system linearized. This results in:

$$\frac{\partial\Psi}{\partial x} = \nabla \times_z \boldsymbol{\tau} - \epsilon_{\mathcal{S}}\Delta\Psi + \epsilon_{\mathcal{M}}\Delta\zeta \tag{2.7}$$

For now, we focus on the simplest Stommel problem by setting $\epsilon_{\mathcal{M}} = 0$. Although this equation can be solved analytically, such solutions often obscure the physical processes behind their derivation. A practical approach is to assume that friction terms are negligible away from the boundary, splitting the solution into two components: the Sverdrupian interior and the boundary layer, where friction becomes significant. This leads to the following formulation:

$$\begin{cases}\Psi = \Psi_{\mathcal{I}} + \Psi_{\mathcal{B}}\\ \frac{\partial\Psi_{\mathcal{I}}}{\partial x} = \nabla \times_z \boldsymbol{\tau}\\ \frac{\partial\Psi}{\partial x} = -\epsilon_{\mathcal{S}}\Delta\Psi_{\mathcal{I}} + \nabla \times_z \boldsymbol{\tau}\end{cases}$$

The goal is to compute the separate solutions and match them asymptotically. This derivation was previously performed by (Wallis) for simple harmonic wind stress and will not be detailed here. It results in an exponentially decaying boundary solution $\Psi_{\mathcal{B}}$. Using the canonical wind stress $\nabla \times_z \tau = -\sin(y)\sin(x)$, the solutions are:

$$\begin{cases}\Psi_{\mathcal{B}} = -2\sin(y)e^{-\frac{x}{\epsilon_{\mathcal{S}}}}\\ \Psi_{\mathcal{I}} = (1+\cos(x))\sin(y)\end{cases} \tag{2.8}$$

The total solution is then:

$$\Psi^{\mathcal{S}} = \left(1 + \cos x - 2e^{-\frac{x}{\epsilon_{\mathcal{S}}}}\right)\sin(y) \tag{2.9}$$

One can observe that this solution does not satisfy all the constraints imposed but does verify, for $\epsilon_{\mathcal{S}} \ll 1$, that $\Psi(x = 0, \pi) \approx 0$. Despite this relaxation of constraints, the model provides a way to handle the boundary layer, which scales as:

$$\hat{\delta}_{\mathcal{S}} = \epsilon_{\mathcal{S}}/\pi, \quad \delta_{\mathcal{S}} = \frac{r}{\beta}$$

It is worth noting that the basin length here is not L but πL. From this, we conclude that if the Gulf Stream originates from the western boundary layer, we should have $\epsilon/\pi \approx 0.01$ [Veronis, part 1], given the same scaling between the Gulf Stream width and the size of the Atlantic Ocean.

Munk's model offers a more nuanced approach when applying the boundary layer method (balancing the friction term with the beta term) and allows handling no-slip and no-normal boundary conditions. However, the precision gained from the no-slip condition may be irrelevant, as it leads to shear flow and instability when considering nonlinear processes. Its derivation is not addressed here. Instead, we will focus on the characteristic western boundary length scale identified in this study:

$$\hat{\delta}_{\mathcal{M}} = \epsilon_{\mathcal{M}}^{\frac{1}{3}}/\pi, \quad \delta_{\mathcal{M}} = \left(\frac{A}{\beta}\right)^{\frac{1}{3}}$$

For geostrophic typical values of

$$\beta = 2e^{-13}\text{cm}^{-1}\text{sec}^{-1}, \quad L = 1e^{8}\text{cm}$$

we obtain $A \sim 10^7\text{cm}^2\text{sec}^{-1}$. In the case of the Atlantic Ocean, the convective term cannot be neglected, leading to significant nonlinearity. Indeed, perturbative methods (see the next section) are known to fail for this range of viscosity values [Stommel, Munk], necessitating full numerical simulations.

One could be motivated to study the "matching case" [1]:

$$\epsilon = \epsilon_{\mathcal{S}} = \epsilon_{\mathcal{M}}^{\frac{1}{3}}$$

This condition results in boundary layers of the same size in both models (see fig.). However, one might question whether this constraint leads to divergent dynamics. Specifically, there is no guarantee that the boundary layer speed will scale similarly in both models. Bryn proposed that the boundary layer speed in the Munk model scales inversely with the boundary layer size, based on the assumption of a constant Reynolds number in the flow:

$$\text{Re} = \frac{V_b\delta_{\mathcal{M}}}{\eta} = \frac{UL}{\eta}$$

where U is the interior Sverdrupian velocity. From this, we infer that even for moderately nonlinear flows, the kinetic energy $\mathcal{K}$ depends primarily on the boundary layer behavior, as the interior flow is assumed to remain unchanged. Hence, it should scale as $\mathcal{K} \propto \delta_{\mathcal{M}}^{-1}$, since the integration is over the boundary layer. This approach provides a quick estimate for $\mathcal{K}$ in the Munk model but is not applicable to the Stommel model.

Indeed, using the same balance between friction and advection in the Stommel model yields:

$$\mathrm{Re}^{\star} = \frac{U}{rL}$$

This results in lower speeds in the boundary layer, which is inconsistent with our case. A more rigorous approach involves integrating v^2 in the boundary layer using $\partial_y(2.8)$[1] for the Stommel model. This yields:

$$\begin{aligned}\mathcal{K}_{\mathcal{S}} &= \int_0^L \int_0^{\delta_{\mathcal{S}}} |\partial_y \Psi_{\mathcal{B}}|^2 \\ &= \frac{\pi}{2\epsilon_{\mathcal{S}}}\left[1 - e^{-2\frac{\delta}{\epsilon_{\mathcal{S}}}}\right]\end{aligned}$$

Notably, only $\Psi_{\mathcal{B}}$ in the boundary is used. This can be justified by observing that $v_{\mathcal{B}}^2$ introduces an $\epsilon_{\mathcal{S}}^{-2}$ dependency, whereas considering the full $\Psi_{\mathcal{S}}$ solution would add only an $\epsilon_{\mathcal{S}}^{-1}$ dependency, which is negligible in this study range. For the Munk model scaling, we use the following western boundary solution under no-slip conditions:

$$\begin{aligned}\Psi_{\mathcal{B}}^{\mathcal{M}} = \sin(y) e^{-x/2\epsilon_{\mathcal{M}}^{1/3}} \Bigg[\cos\left(\frac{\sqrt{3}x}{2\epsilon_{\mathcal{M}}^{\frac{1}{3}}}\right) + \\ \frac{1 - 2\epsilon_{\mathcal{M}^{\frac{1}{3}}}}{\sqrt{3}} \sin\left(\frac{\sqrt{3}x}{2\epsilon_{\mathcal{M}}^{\frac{1}{3}}}\right) \Bigg]\end{aligned} \tag{2.10}$$

This yields the following kinetic energy:

$$\begin{aligned}\mathcal{K}_{\mathcal{M}} = \frac{\pi}{2\epsilon_{\mathcal{M}}^{\frac{1}{3}}} \Bigg[\frac{5}{4} - e^{-1} - \\ \frac{e^{-1}}{4}\left(\cos\sqrt{3} + \sqrt{3}\sin\sqrt{3}\right)\Bigg]\end{aligned} \tag{2.11}$$

It is evident that the scaling aligns with the prediction from Reynolds arguments. Hence, even though $\mathcal{K}^{\mathcal{S}} \propto \mathcal{K}^{\mathcal{M}} \propto \delta_{\mathcal{SM}}^{-1}$, the kinetic energy in the boundary layer (the main contributor in low-nonlinearity scenarios) is nearly three times higher in the Munk model, leading to higher transport for the same boundary layer size.

We emphasize that the boundary conditions for the Munk model differ from those used in the Stommel model, which could influence the scaling. This imprecision is significant but not overly concerning, as boundary conditions vary across oceans; yet, the same phenomenon is observed. Additionally, only the boundary solution, the leading order in the boundary layer, was considered. However, Ψ is a combination of Sverdrupian and boundary stream functions, which should influence the kinetic energy ratio. This significantly impacts the dynamics studied, as transport in the Munk model will be higher for the same boundary layer width.

B. Non-linear system study

Assuming non-linear term to be sufficiently small, we can applly the so-called perturbative methods by developing the solution in a power series of the Rossby number $\mathcal{R}$. This method provides us a qualitative understanding of the non-linear term effect on northern currents intensification in the boundary layer, and how the solution is distorted by the convective term. The derivation has already been done by [Veronis], and briefly is briefly explained in this section. Let's consider the following development of the stream function :

$$\Psi = \Psi_0 + \mathcal{R}\Psi_1 + \cdots$$

At the first order injecting this development in the linear system (2.7) we get

$$\frac{\partial \Psi_1}{\partial x} + \epsilon_{\mathcal{S}} \Delta \Psi_1 = \mathcal{J}(\Psi_0, \zeta_0) \tag{2.12}$$

substituting the expression of Ψ_0 (2.14), and applying a boundary layer stretching (see Wallis for a simple application on a harmonic wind stress), we finally obtain a boundary solution for (2.12)9, recalling $\xi = \frac{x}{\epsilon_{\mathcal{S}} cal}$:

$$\Psi_1^{\mathcal{B}} = -\frac{2\xi\mathcal{R}}{\epsilon_{\mathcal{S}}^2}\sin(2y)e^{-\xi} \tag{2.13}$$

Furthermore, As the main contribution of the non-linearity has to be in the boundary layer (where the gradient of speed is the higher), we can just add this non-linear contribution to the previous Stommel boundary solution, leading providing a northern intensification of the streamfunction, and so a increasing velocity near the northern boundary.:

$$\Psi = \Psi^{\mathcal{S}} - \frac{2\xi\mathcal{R}}{\epsilon_{\mathcal{S}}^2}\sin(2y)e^{-\xi} \tag{2.14}$$

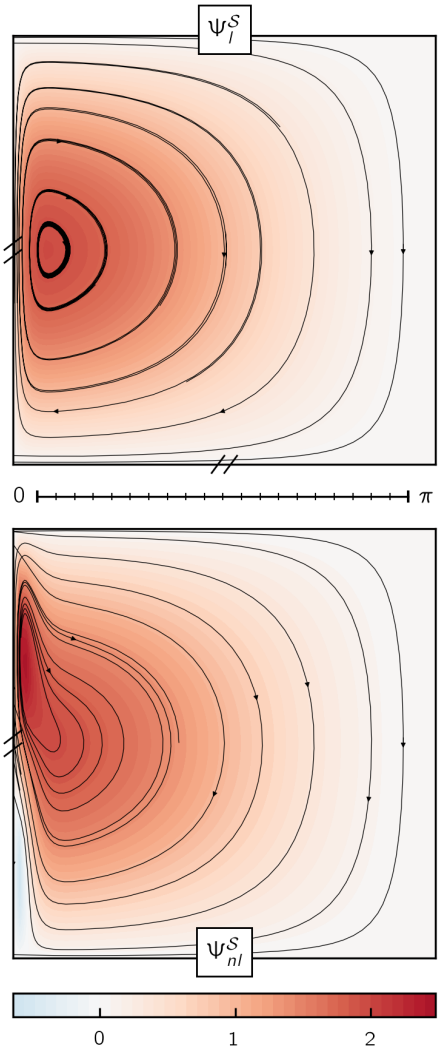

Figure 2.1 – At the top, contour plot of the linear stommel solution $\Psi_l^{\mathcal{S}}$, with $\epsilon_{\mathcal{S}} = 0.05$. At the bottom, the perturbed stommel solution at the bottom : $\Psi_{nl}^{\mathcal{S}}$ for $\epsilon_{\mathcal{S}} = 0.05$ and $\mathcal{R} = 0.005$. Streamline are represented in black plain lines

The form of 2.14 will lead to a polewards shift of teh center of gyre with a longitude wise antysymetric structure of the streamfunction in the boundary layer (see 2.1). If we take a quick glance at the ratio of the norm :

$$\left|\frac{\Psi_1^{\mathcal{B}}}{\Psi_{\mathcal{B}}^{\mathcal{S}}}\right| = \frac{\mathcal{R}}{\epsilon_{\mathcal{S}}^2}, \quad x = \delta_{\mathcal{S}}$$

[1] Since Ψ vanishes at the boundary, there is no normal flow.

This suggest the existence of an inertial boundary layer (Charnet layer), where the particles inertia is balanced by the coriolis force.

$$\delta_{\mathcal{I}} = \left(\frac{U}{\beta}\right)^{\frac{1}{2}} \propto \mathcal{R}^{\frac{1}{2}}$$

C. Inertial layer study

When this length scale is the same order that the frictionnal boundary layer, it will strengthend the dynamic at stake with a northward advection in the boundary layer (where the transport is the higher) of the gyre. For non-linear regime this advection will cause the westard boundary layer to reach the north boundary causing oscillations in the vorticity (see fig 2.2).

Indeed, one can notice that the bonudary layer act as a negative vorticity damping layer, in the non-linear regime this damping will act longer because of inertia, causing a positive vorticity zone.

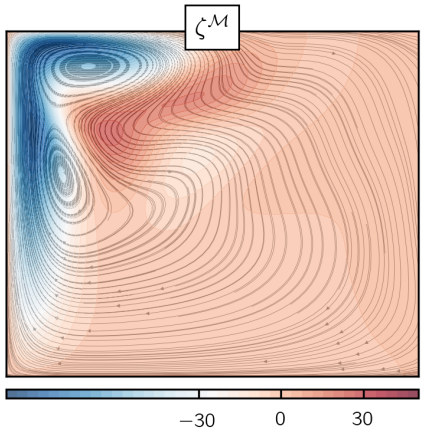

Figure 2.2 – Western boundary layer vorticity plot for the Munk model using $R = 8e^{-3}$ and $\epsilon_{\mathcal{M}} = 1e-3$, with underlying stream lines

One can see that as the consequences of vorticity conservation when we advect a parcel of fluid:

$$\int_{\mathcal{D}} \boldsymbol{v}\cdot\nabla\zeta\, d\mathcal{D} = \int_{\mathcal{D}} \nabla(\boldsymbol{v}\zeta) d\mathcal{D} = \int_{\partial\mathcal{D}} \zeta\boldsymbol{v}\cdot\boldsymbol{n}\, d\partial\mathcal{D}$$

Since the stream function Ψ vanish on the boundaries, there is no normal flow we finally get :

$$\int_{\mathcal{D}} \boldsymbol{v}\cdot\nabla\zeta d\mathcal{D} = 0 \tag{2.15}$$

The negative vorticity zone being increased with the northward advection, we need a positive vorticity zone to compensate. The same property can be unearthed for the kinetic energy K as we will see further.

To tackle non-linear and highly non-linear regime correctly we must use numerical methods. One can propose to study the steady non-linear regime using newton solver, but it's not clear that the dynamic will always reach a steady states, veronis obtained accurately steady dynamic even for highly non-linear case but this was only restricted to the Stommel model. Bryan when solving numerically the non linear model unearthed some unsetady dynamic, that could be related to the discretization limitations.

Hence to be very general we will use a time dependant approach starting from rest.

NUMERICAL IMPLEMENTATION

I. finite difference formulation

To solve the numerically 2.5, we discretized a rectangular bassin $\mathcal{D}$ given a regular $N-1$ gridded interval with spacing :

$$\Delta x = \Delta y = \frac{\pi}{N-1}$$

We studied the no-normal flow ($\Psi_{\mathcal{D}} = 0$) with free slip boundary condition (this prevents any shear flows instabilities from no-slip consideration).

In the interior we computed the spatial derivatives using a simple order 2 centered difference method, this ensure stability for sufficiently smooth fields(NEED to filter frequencies) :

$$\partial_x\Psi = \frac{\Psi_{i+1,j} - \Psi_{i-1,j}}{2\Delta x}$$

For the time dependancy we used the same leapfrog-like scheme :

$$\partial_t\Psi = \frac{\Psi^{n+1} - \Psi^{n-1}}{2\Delta t}$$

This temporal scheme can introduce introduce instability at high frequency, $1/2\Delta t$ that can be excite by simple roundings errors (some suggests to introduce some filtering (Robert-Asselin), or damping to avoid this problem. In the stommel model the drag is a quite harsh damping that act equally on all frequency, in addition to that we can show that using leapfrog scheme the dragging term leads to an unstable exponentially growing unstable mode.

Indeed let's consider the following discretization of (2.5).

$$\frac{\zeta_{ij}^{n+1} - \zeta_{ij}^{n+1}}{2\Delta t} + \mathcal{R}\mathcal{J}_{ij}^{n} = -\epsilon_{\mathcal{S}}\zeta_{ij}^{n} + \epsilon_{\mathcal{M}}\mathcal{L}\zeta_{ij}^{n} + \nabla\times_z\boldsymbol{\tau} \tag{3.1}$$

using the foloowing expression for $\mathcal{L}$ and $\mathcal{J}$:

$$\begin{aligned}
\mathcal{L}\zeta_{ij} &= \frac{\zeta_{i+1,j} + \zeta_{i-1,j} + \zeta_{i,j+1} + \zeta_{i,j-1} - 4\zeta_{ij}}{\Delta x^2}\\
\mathcal{J}_{ij}^{n} &= \left[(\Psi_{i+1,j+1}^{n} - \Psi_{i-1,j+1}^{n})\zeta_{i,j+1}^{n}\right.\\
&\quad \left. - (\Psi_{i+1,j-1}^{n} - \Psi_{i-1,j-1}^{n})\zeta_{i,j-1}^{n}\right]\\
&\quad - \left[(\Psi_{i+1,j+1}^{n} - \Psi_{i+1,j-1}^{n})\zeta_{i+1,j}^{n}\right.\\
&\quad \left. - (\Psi_{i-1,j+1}^{n} - \Psi_{i-1,j-1}^{n})\zeta_{i-1,j}^{n}\right]
\end{aligned}$$

A. Jacobian formulation

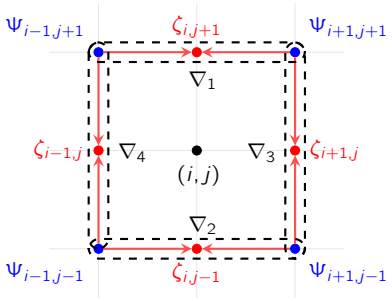

Figure 3.1 – Illustration of the Jacobian computation for the vorticity equation. We sketched in blue the points used for the streamfunction and in red for the vorticity

For the simplicity of the next study we will write this jacobian in this reducted form :

$$\begin{aligned}
\mathcal{J}_{ij} &= \nabla_{ij}^{1}\zeta_{i,j+1} - \nabla_{ij}^{2}\zeta_{i,j-1}\\
&\quad -\nabla_{ij}^{3}\zeta_{i+1,j} + \nabla_{ij}^{4}\zeta_{i-1,j}
\end{aligned} \tag{3.2}$$

This Arakawa like Jacobian form ensure the vorticity and kinetic conservatin through advection [2–4]. We already studied that for the vorticity case (eq. 2.15). For the kinetic energy we can consider the following integration :

$$
\begin{aligned}
2\mathcal{K} &= \int_{\mathcal{D}} |\boldsymbol{v}|^2 \\
&= \int_{\mathcal{D}} |\nabla^T \Psi|^2 = \int_{\mathcal{D}} |\nabla \Psi|^2 \\
&= \underbrace{\int_{\mathcal{D}} \nabla \cdot (\Psi \vec{\nabla} \Psi)}_{\text{0 from Ostrogradski theorem}} - \int_{\mathcal{D}} \Psi \Delta \Psi \\
&= -\int_{\mathcal{D}} \Psi \zeta
\end{aligned}
$$

We can then show very easily the conservation of the kinetic energy through advection noticing that : $\boldsymbol{v} \cdot \nabla \Psi = 0$, using the same arguments as before:

$$\int_{\mathcal{D}} \boldsymbol{v} \cdot \nabla(\Psi \zeta) = 0 \tag{3.3}$$

To show that equations (2.15, 3.3) are verified for this discretized Jacobian :

$$\sum_{ij} \mathcal{J}_{ij} = 0 \quad , \quad \sum_{ij} \Psi_{ij} \mathcal{J}_{ij} = 0$$

The first equality is trivially provided noticing that the $\nabla^1_{i,j}, \nabla^2_{i,j+2}$ terms cancel each other as well as the $\nabla^3_{i,j}, \nabla^4_{i+2,j}$ terms. For the second equality this is a little but more tricky and we have to notice that the cancellation will involve four terms :

$$
\begin{aligned}
\Psi_{i,j}\nabla^1_{ij} + \Psi_{i,j+2}\nabla^2_{i,j+2} + \Psi_{i-1,j+1}\nabla^3_{i-1,j+1} \\
+ \Psi_{i+1,j+1}\nabla^4_{i+1,j+1} = 0
\end{aligned}
$$

This implicit implies that our grid grise has to be divisible by 4.

B. Friction stability

The von-Neumann analysis leads to the consideration of the following harmonic wave functions :

$$\zeta = A\rho e^{ikx}, \quad \rho = e^{iwt}$$

If we restrict the study to the friction terms we get :

$$\rho^2 + 2\Delta t \epsilon_{\mathcal{M}} \rho - 1 = 0 \tag{3.4}$$

From the same reasoning as befire (encapsulating under the nabla) This will lead to one unstable mode whatever the ρ we choose :

$$\rho = \Delta t \epsilon_{\mathcal{M}} + \sqrt{(\Delta t \epsilon_{\mathcal{M}})^2 + 1} < -1$$

One way to adress this issue we can simply consider the previous time step for the friction term (One can also use the same time centered scheme for the friction term, VERONIS). This will simply give :

$$\rho = \sqrt{1 - \epsilon_{\mathcal{M}} \Delta t} < 1$$

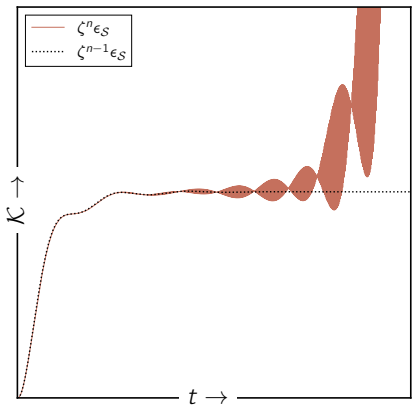

Figure 3.2 – Kinetic Energy Overview of the instability induced by the central differences by using a centered friction term detailed in the previous section. This is not greatly noticeable for reasonable value of the $\epsilon_{\mathcal{S}}$ and $\mathcal{R}$

The stability will then be ensure for the friction term at least. This final consideration leads to our numerical scheme

$$
\begin{aligned}
\frac{\zeta^{n+1}_{ij} - \zeta^{n+1}_{ij}}{2\Delta t} + \mathcal{R}\mathcal{J}^n_{ij} = -\epsilon_{\mathcal{S}} \zeta^{n-1}_{ij} + \epsilon_{\mathcal{M}} \mathcal{L} \zeta^n_{ij} \\
+ \nabla \times_z \boldsymbol{\tau}
\end{aligned} \tag{3.5}
$$

C. CFL-like considerations

The harmonic viscosity we consider in the Munk model will canonically lead to the following restriction on the time stepping size :

$$\Delta t < \frac{\Delta x^2}{4\epsilon_{\mathcal{M}}}$$

For the Stommel term the restriction is way more relaxed, since the term is not a diffusion term but a drag term. We can then consider the following restriction :

$$\Delta t < \frac{1}{\epsilon_{\mathcal{S}}}$$

Regarding the advection term, it will classically leads to the following CFL conditions :

$$\Delta t < \frac{\Delta x}{2 \max|\boldsymbol{v}|}$$

RESULTS & DISCUSSION

In this chapter we will exploit the simulations results for the stommel and the munk model in a wide range of parameter. We will verify the scaling of the boundary layer and of the Kinetic energy, and study the non-linear regime in both model for comparable size of the boundary layer.

I. Boundary layer

As we depicted previously Stommel and Munk model do not leads to the same dymanics for the matching case :

$$\epsilon^{\frac{1}{3}}_{\mathcal{M}} = \epsilon_{\mathcal{S}}$$

However one can compare if the boundary layer width is preserved by the numerical integration. This is done by comparing the normalized meridional velocity profiles in the 4.1 using a the linear case $\mathcal{R} = 0$.

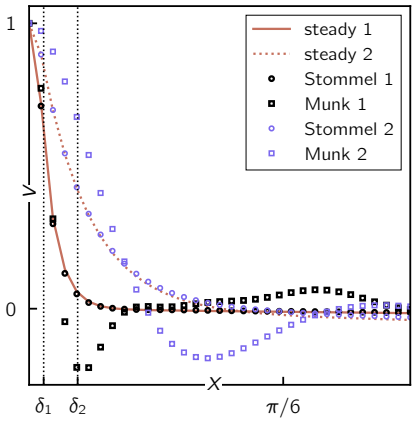

Figure 4.1 – Normalized meridional average velocity profile after 4000 iterations (corresponding to $200(\beta L)^{-1}$s) for $\epsilon^{1/3}_{\mathcal{M}} = \epsilon_{\mathcal{S}} = 0.03$ or the black points and w $\epsilon^{1/3}_{\mathcal{M}} = \epsilon_{\mathcal{S}} = 0.1$ for the blue points. Both simulations are tackled using $\mathcal{R} = 0$ with free slip boundary conditions. The steady solutions refers to the previously calculated linear solutions for the stommel model (eq. 2.8).

One can see that the numerical scheme converge quite well to the steady solutions. With quite a good agreement between the Munk and the stommel boundary layer width. One notice that for the Munk case the bonudary layer seems wider for both sets of parameters, which will leads to higher transport concomitantly with the higher kinetic energy in the boundary layer (see subsection A). We will show further that the width of the boundary layer follows

the scaling we predicted $\delta_{\mathcal{S}} \propto \epsilon_{\mathcal{S}}$ and $\delta_{\mathcal{M}} \propto \epsilon_{\mathcal{M}}^{1/3}$ in the next section.

II. Dynamics

The study of the dynamic of the two model revealed interestings points about the transcient aspect of the solutions, the difference of boundary transport betweeen the two models. Some investigations have been done regarding the transcient aspect of the solutions in Veronis and Bryan works.

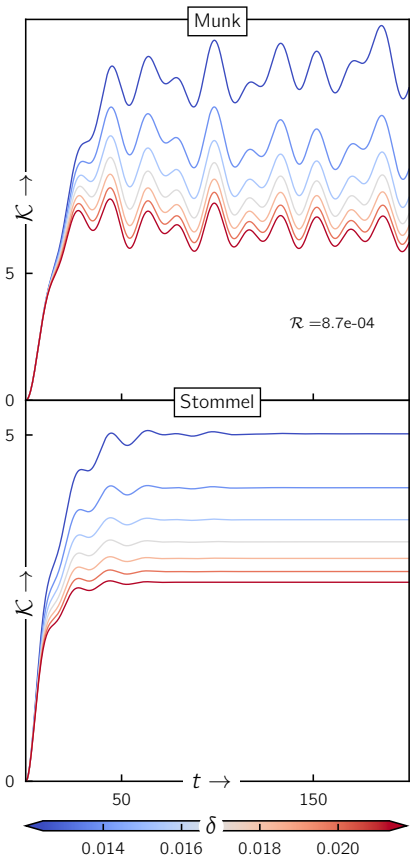

Figure 4.2 – Kinetic Energy plot for the several boundary layer size in the matching case : $\epsilon_{\mathcal{M}}^{1/3} = \epsilon_{\mathcal{S}}$. The maximum Reynolds number we reached is $Re \sim 30$, as opposed to bryan who reached $Re \sim 60$. However one can note that our boundary layer is relatively π times smaller which corresponds in the Byran case to $Re \sim 90$

However, they do not lead to the same results. Indeed, Veronis who used the Stommel model in his study explained that his solutinons did not unearth trasncient behavior as opposed to Bryan work. He justified that saying that Bryan used a no Slip boundary condition at the border which implied a strong inflection point and shear-flow instabilities that can be responsible for this transcient aspect. However, Bryan explains this as free rossby waves propagation in the rectangular bassin and demonstrate this with assurance.

In our simulations we observed this transcient process in both, stommel and Munk Model. However we will see that in the stommel model the trasncient behavior vanish rapidely. Whereas in the Munk model the transcient behavior is clearly present. This is a quite interesting point that we will discuss further. And seems to not be related to the numerical implementation as discussed by Veronis.

A. Rossby solutions

Neglecting the friction and the advection (2.5) becomes simply :

$$\partial_t \zeta + \partial_x \Psi = 0$$

From this very simple equation we can derive the following free rossby wave adimensionalized dispersion relation in the fourrier space using normal fourrier modes :

$$\Psi = \Psi_0 e^{i(k_x x + k_y y - \omega t)} \tag{4.1}$$

The dispersion relation follows.

$$\omega = \frac{k_x}{k_x^2 + k_y^2} \tag{4.2}$$

Bryan proposed a cleaner approach that leads to truncation of an initial guess in slighly more complicated dispersion relation. If we add the friction term to the equation we will derive the following dispersion relation for the Munk case :

$$\partial_t \zeta + \partial_x \Psi = 0$$

$$\omega = \frac{k_x}{k_x^2 + k_y^2} + i\epsilon_{\mathcal{M}}(k_x^2 + k_y^2) \tag{4.3}$$

For the Stommel case the dispersion relation will be :

$$\omega = \frac{k_x}{k_x^2 + k_y^2} + i\epsilon_{\mathcal{S}} \tag{4.4}$$

From this simple study one can see that the friction in the Stommel case implies a damping of transcient solutions. Which is not always the case in the Munk case, indeed nothing ensures that $\boldsymbol{k} \in i\mathbb{R}$, on the contrary it should have a real part.

a) Munk damping study

This damping is evident in the fig.4.2, where the same modes are quickly damped in stommel model and not in the Munk model. The period of the wave is of the order of $T \sim 40(\beta L)^{-}1s$ which corresponds exactly to the period Bryan unearthed $T \sim 44(\beta L)^{-}1s$

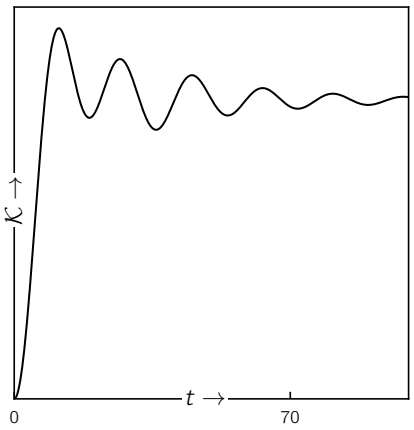

(a) – Stabilized Kinetic energy plot time evolution

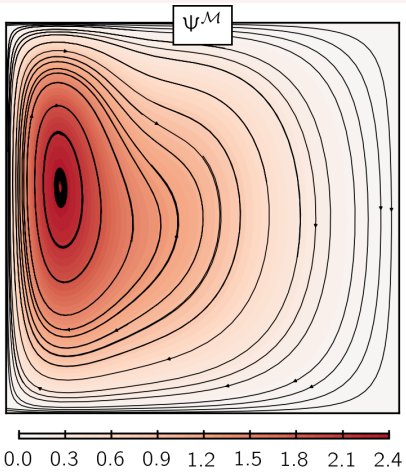

(b) – Steady state Ψ contour plots taken at last time step

Figure 4.3 – Simulations plots for $\epsilon_{\mathcal{M}} = 6e-3$ and $\mathcal{R} = 8e-3$. Corresponding to $\delta \approx= 0.1$, which is not feasible in the reality

Here we discussed a interesting case with $\delta_{\mathcal{M}} = 0.01$, in order to match the characteristic Gulf stream width. However, we will show further that, in addition to add numerical complexity to have a well defined boundary layer, this is crudely limiting the rossby number $\mathcal{R}$. Indeed for the same boundary layer size if we increase the rossby number higher

than $Re \sim 60$ the boundary layer fails to damp efficiently the flows and the existence of a steady state is seriously compromised (as we can see in the fig.4.3).

However if we allow the boundary layer to be bigger in the Munk model we can deal with bigger northern intensification phenomena. That's actually matching the Stommel dynamics. In this case it appears that the Rossby free waves can be damped by the Munk friction term (see fig.**??**).

This damping in the Munk problem comes along with other stability problem that are well known for the Munk problem [3, 5, 6]. It is well known that Munk dynamics presents some instability as the western boundary depending on the Reynold number.

The stability range is assume to be between 25-100 for most of the problem. Here we can show that it is really hard to obtain stable results near Re $\sim$ 60, Bryan attributes that to unsufficient discretized boundary layer size leading to not enough damped dynamic and divergent behavior.

b) Munk divergence study

This idea is quite reasonable however, we replicate the same scheme as bryan and pushed the discretization further and we still obtained unstable solution. Bryan used a [1,1] domain with $N = 40$ points, we used a π times domain (the boundary layer width will also be multipled by π) and $N = 128$ points, and we still not converge to a steady oscillatory state as we can see in fig.4.4.

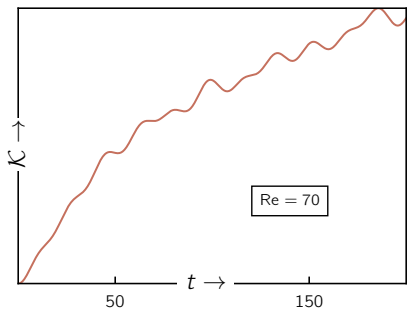

Figure 4.4 – Energy time evolution for Re = 75, using $\epsilon_{\mathcal{M}} = 1.2e^{-5}$ and $\mathcal{R} = 9e^{-4}$

To possibly understand and strengthened, complete the Bryan argumentation, one can ask if this instability is only numerically originated and if it is not a physical expected results.

c) Munk instability study

In the following section we will try to explain how this instability occures in the Munk model using the spectral analysis we did before. Indeed this special dispersion relation we obtained in the linear Munk case without carrying about the advection term can be pushed further than it can be possibly not dissipative. For this we propose a study of $\mathrm{Im}\,\omega$, depending on k_x.

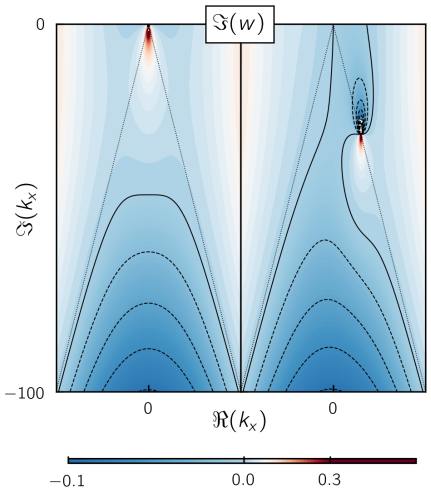

Figure 4.5 – Imaginary Frequency response contour plot over the k_x for two different k_y. *On the left :* we used a purely real $k_y = 1$. *On the right :* we used a complex $k_y = 30(1 + i)$. The black plain line contour stands for the 0 level, hence it is the stability threshold of our model. The dashed contour line are negative contour.

In this study we will assume the following points. First the $\mathrm{Im}(k_x) \in \mathbb{R}^-$. This follows simply from the fact that there is no exponentially growing spatial scale in our study. Secondly, we will assume that at the begiining of our study the k_y wave vector is relatively small indeed the smallest length scale generated by our study are located in near the boundary layer as dicussed in the positive vorticity section, and at the boundaries the y-length scale are expected to be quite important due to our square box.

The action of the advection term is then to mix the x and y length scale leading to increasing real part of k_y with time. This is quite contradictory with a 2D geometry where an inverse energy cascade should favorites big scales, however as explained by [7] as long as the flow is not free and limited by a boundary it will create small scale proportionally to the Re.

In addition to that mixing of small scaled by the advective term, one could remarks that the unstability occurs when the main flow structures is reaching the north limit of our domain, i.e when the boundary layer spread on the north side. This will results in the considerations of a $\mathrm{Im}(k_y) \neq 0$, indeed a damping effect as to be considered in the north boundary layer.

This will finally result in presence of high valued complex k_y wave vector. To understand what is the impact of this k_y values on the spectrum, we plotted $\mathrm{Im}(w)$ for two interesting k_y values. Stability is ensure at positie values of $\mathrm{Im}(w)$ and the instability occured for negative values.

First, we recover the Bryan numerical constraints for all cases : the boundary layer needs to be sufficiently resolved. Indeed, let's say the boundary layer is of the order :

$$\delta_{\mathcal{M}} = \epsilon_{\mathcal{M}}^{\frac{1}{3}} \sim 6.10^{-}2$$

The associated imaginary k_y will be of the order of $\frac{2\pi}{\delta_{\mathcal{M}}}$. If our resolution is not enough we will not provide sufficiently high k_x wave number leading to negative $\mathrm{Im}(w)$ and instability growing. We recover the fact that if the boundary layer is too thin to be numerically represented the friction is not enough important to dissipate wind stress.

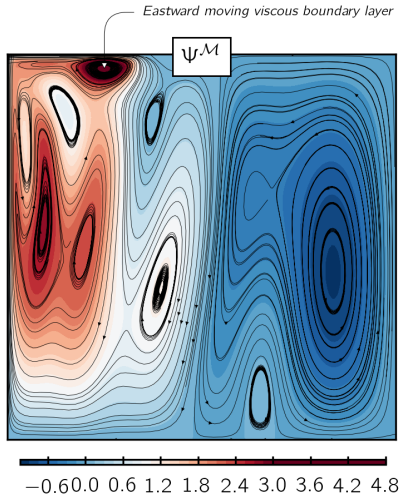

Figure 4.6 – Contour plot of Ψ with streamlines in plain black, for a Re = 60 at $t = 100(\beta L)^{-1}s$ with $\epsilon_{\mathcal{M}} = 1.5e^{-5}$. Small scales structures appear in both y and x direction with a strong eastward boundary layer flow at the northern boundary with a typical $k_x \sim 1-10$, corresponding to an unstable mode.

Furthermore the more interesting thing we have to notice, is an other instability zone that is occuring when the boundary layer span over the north

boundary, leading to negative $\mathrm{Im}(x)$ for a all span of big scales, corresponding to eastward traveling structure in the northern newly created viscous boundary. This eastward intensification of the flow is clearly depicted in the fig.4.6.

This unstable mode is not numerically originated and do not leads to a stable steady flow, indeed as long as the wind stress is apply the eastward boundary layer will still exist and will continue to nucleate this kind of northern eastward moving structures.

For the following part we propose to delve into the hypothesis we made to explain this eastward intensification at the northern boundary for the Munk model. First we assumed that small scales have an increasing presence due to the boundary layer inversely proportionally to Re. Then we sum up the action of the advective term, by a mixing in y and x direction of small scale. And then we finally suppose that the westward boundary layer will progressively go northward, leading to complex k_y.

The decreasing scales in the boundary layer is a results of an equilibrium between the viscous force and the advective force. This will lead to :

$$v\partial_x v \sim \epsilon_{\mathcal{M}} \partial_{xx} v$$
$$\frac{v^2}{\delta} \sim \epsilon_{\mathcal{M}} \frac{v}{\delta^2}$$
$$\delta \sim \frac{L}{\mathrm{Re}}$$

Here we can see that the domain should be limited so that small scales can appear in a 2d flow. At planetery scale it is generally admit that the forward energy cascade is mediated by planetary vorticity gradients. This is a charcteristic from a barotropic flow, but if we consider a more baroclinic flow this inverse cascade should vanish due to the 3d geometry introduced. This small scales are then distributed over both directions as we can see in the fig.4.8 where we computed the power spectrum over the whole boundary layer in the y direction limited to the nyquist frequency computed with an appropriate Hann window.

The power spetrum spread with the Re and the time as expected(4.7, 4.8). In addition to that one could notice that we have an increasing contribution for high Re. This should be related to the fig.4.9, where we emphasize the northward concentration of the boundary layer leading to small scales.

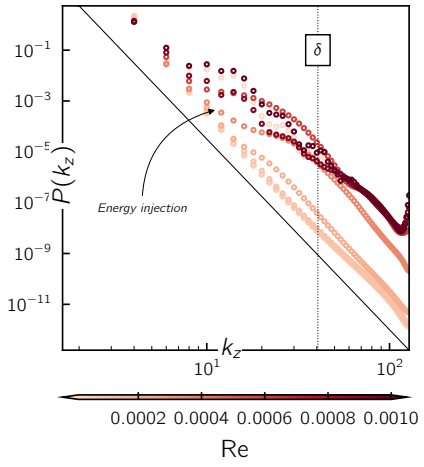

Figure 4.7 – Re dependant power spectrum fo with $\epsilon_{\mathcal{M}} = 1.5e^{-5}$, average over the 500 last time steps. The black plain line stand for a power law of $k_z^{-7.5}$

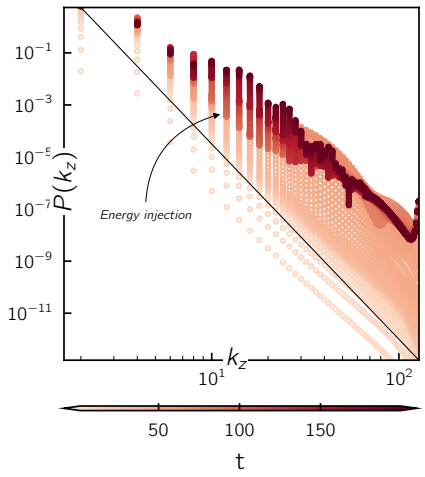

Figure 4.8 – time dependant power spectrum for $Re = 60$, with $\epsilon_{\mathcal{M}} = 1.5e^{-5}$. The black plain line stand for a power law of $k_z^{-7.5}$

This Spetrum study unveiled an interesting energy cascade way stronger than the Kolmogorov one $k^{-\frac{5}{3}}$, that seems to be affected by an injection of energy of typical scale $\frac{1}{\delta_{\mathcal{M}}}$ however we recover for high frequency the natural energy cascade. This is in agreement with the Veronis argument [3] stating the we cannot generate length scale smaller than the boundary layer.

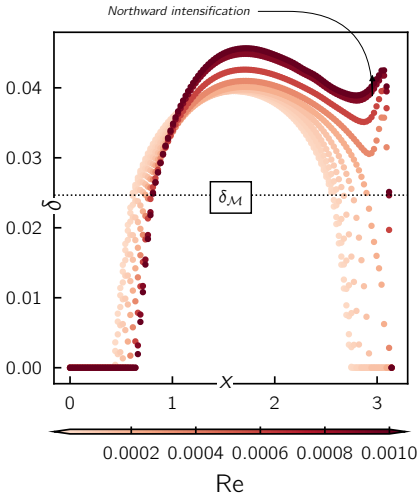

Figure 4.9 – Western Boundary layer width evolution with the Reynolds number with $\epsilon_{\mathcal{M}} = 1.2e^{-5}$. The black dotted line stands for the theoritical width of the boundary layer.

To put it in a nutshell this instability study explains why there is no assurance to have a steady states if we study strong convective flow.

We observe the same kind of behavior for very strong convective flow for the stommel model , however in our simulations it is always converging. We plotted bellow the frqency response of the Stommel model , and it is easy to understand from our previous argumentation that in the same conditions this model will lead to stable solutions.

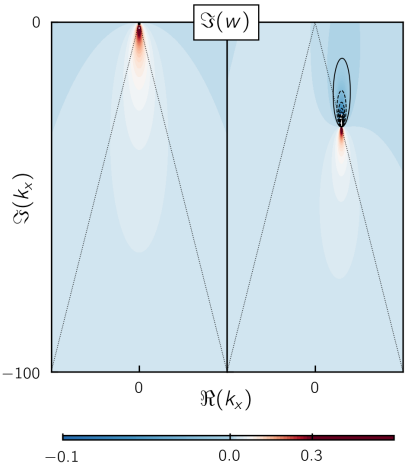

Figure 4.10 – Imaginary Frequency response contour plot over the k_x for two different k_y. *On the left :* we used a purely real $k_y = 1$. *On the right :* we used a complex $k_y = 30(1+i)$. The black plain line contour stands for the 0 level, hence it is the stability threshold of our model. The dashed contour line are negative contour.

From now when studying advective non-linear regime we will focus on the Stommel model. Indeed it allows to reach realistic boundary layer size, whereas to study Munk model we need to introduce too wide boundary layer compared to realistic gulf stream width.

B. Low non-linear regime

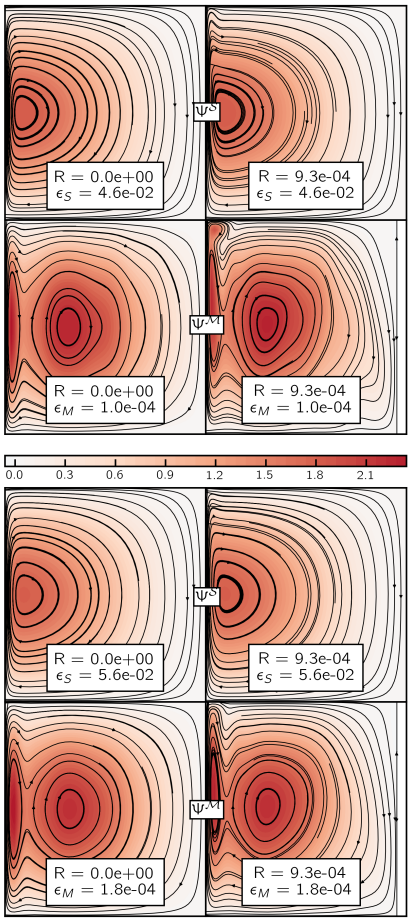

Figure 4.11 – Ψ contour plots with streamlines in both Munk and Stommel case for two boundary layer width in the non-linear and linear case

For the low non-linear regime one has to keep in mind our previous perturbation study with a small rossby number leading to northern intensification of the boundary layer where the transport is the highest. As we can see for the fig.4.11. We recover the linear perturbed solution in the Stmmel case. The Munk model leads to the same northern intensification phenomena, however in our figure Ψ in not average over the rossby period, so we do not recover the stommel typical structure. One can notice as predicted that the boundary transport is bigger in the Munk case as predicted by our previous Kinetic study (it is more precisely study in the fig.4.12).

In the context of low non-linear regime we can see if the scaling for the kinetic energy over the boundary layer size is verified for both model **??**. We also recover the fact that kinetic energy is not affected by the advection, except for a very small boundary layer where the model failed to converge properly, for high $\mathcal{R}$ number.

We also recover the fact that for the same theoritical boundary layer width the system does not unearthed the same dynamics with a factor $\mathcal{K}^{\mathcal{M}}/\mathcal{K}_{\mathcal{S}} \sim 2$, assessing the theoretical approach we did previously.

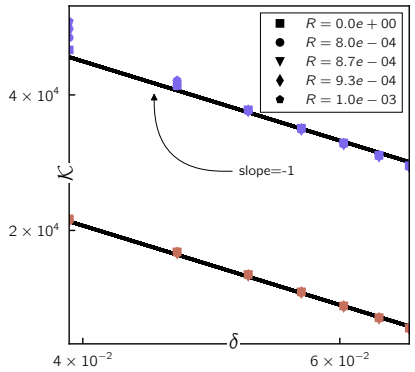

Figure 4.12 – Kinetic Energy over the boundary layer width for the stommel and the Munk model. The black plain line stands for the theoretical scaling δ_S and $\delta_{\mathcal{M}}$

C. High non-linear regime

As explained previously we will focus in this case to realistic boundary layer size, and to do so we will need the stability of the Stommel scheme. We could have also used the Munk model with a bigger boundary layer and an relatively small inertial boundary layer, stating that the boundary layer should be inviscid rather than frictious (controlled by $\delta_{\mathcal{I}}$).

a) Fofonoff solution

For High non linear regime the assymetry we imposed with the frictional layer is progressively lost. and we recover a east-west symetry characteristic of the Fofonoff solution. Indeed the strong advection allows a east boundary layer and a fully inertial interior, that breaks our previous assymptotic matching. This can be traduced by the following requirements for the flow :

$$\mathcal{J}(\Psi, \zeta + \beta y) = 0 \tag{4.5}$$

One can show that for sufficiently low $\mathcal{R}$, this leads to the following Ψ solution. The detailed of the demonstration are given by [1] and will not be tackled here. The main ideas are the same as before with an inertial boundary layer matching with an inertial interior.

$$\Psi = U(y - y_0)\left[1 - e^{\frac{x}{\delta_{\mathcal{I}}}} - e^{\frac{x - x_E}{\delta_{\mathcal{I}}}}\right] + U(y_0 - y_N)e^{-(y_n - y)/\delta_{\mathcal{I}}} + Uy0e^{-y/\delta_{\mathcal{I}}} \tag{4.6}$$

With $\delta_{\mathcal{I}}$ the previously defined inertial boundary layer size and x_E, y_N the east and north boundary position. This solution as a very particular east-west symmetry that we should emphasize.

This stands as a quite extreme case of flow were inertial effect are dominant. Hence, we tested stommel model to see if it was able to recover this flow properties at high rossby number, where we recovers east-west symmetry.

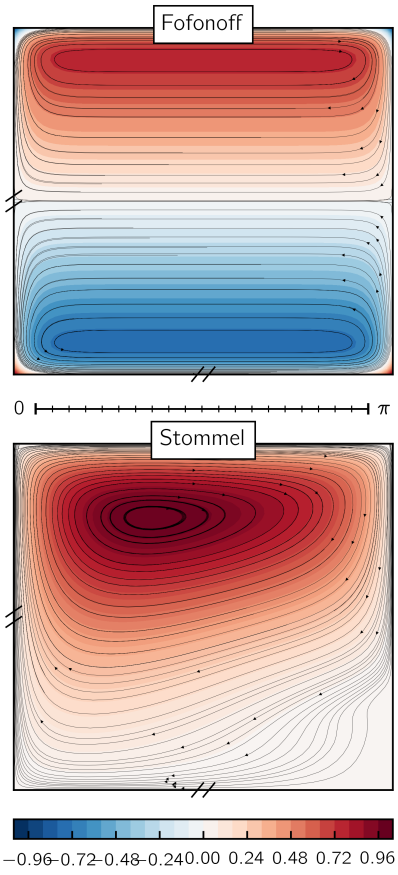

Figure 4.13 – Normalized Stommel model solution at the bottom and normalized Fofonoff solution at the top.

We recoverd quite the same kind of dynamics in the high Rossby number case as highlighted by Veronis [3], despite the fact that there is no boundary layer on the west and east side in our case.

III. Wind stress distribution

Munk proposed to use real wind stress distribution of wind rather than a simple negatiive sinusoidal curl.

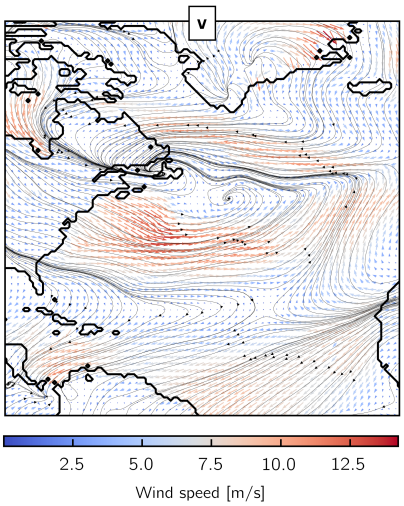

(a) – Global Atlantic velocity fields with streamlines from copernicus program [8]

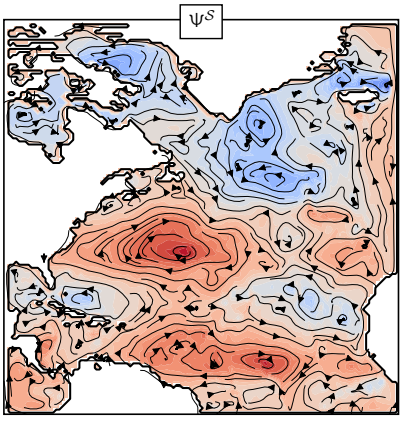

(b) – Global Atlantic solutions for stommel model with $\epsilon_S = 0.02$ and $\mathcal{R} = 9e^{-4}$

Figure 4.14 – Realistic wind stress distribution and stommel model solution

As an applying case we done that using the copernicus programs [8] and we averageover 20 global measurements of the wind stress across the 2019 year in the atlantic ocean. We then applied this wind stress distribution to our model with a masked 256 over 256 grid to tackle finely the coasts boundaries. As we can see on the fig.4.14b the stommel model presents some interesting behavior, where we extract some important features of the global ocean behavior. Indeed we recover subtropical anti-cyclonic and subpolar cyclonic gyres. We also recover the gulf stream western intensification and the. However we did not recover a broader and weaker stommel like internal flow.

CONCLUSION

In this study, we have conducted a comprehensive numerical investigation into the phenomenon of western boundary current intensification in wind-driven ocean models, focusing on the classical Stommel and Munk models. Our primary objective was to understand the dynamics and scaling laws governing these currents, particularly in the context of the Gulf Stream and similar oceanic features.

We began by revisiting the theoretical foundations laid by Stommel and Munk, highlighting the key differences in their approaches to frictional mechanisms and their implications for boundary current intensification. Through a detailed derivation and adimensionalization of the governing equations, we established a framework for numerical simulations.

Our numerical implementation employed a finite difference formulation with a leapfrog-like temporal scheme, ensuring stability and accuracy in the discretization of the vorticity and streamfunction equations. We carefully addressed potential numerical instabilities, particularly those arising from the friction terms, and validated our approach against known analytical solutions.

The results of our simulations revealed several important insights:

First we confirmed that the width of the boundary layer scales as predicted by the theoretical models, with the Stommel model exhibiting a narrower boundary layer compared to the Munk model. This difference in boundary layer width has significant implications for the transport properties of the currents.

Secondly our simulations verified the theoretical scaling laws for kinetic energy in both models. We observed that the Munk model consistently exhibited higher kinetic energy in the boundary layer, leading to greater transport for the same boundary layer width.

We also explored non-linear regime, we observed a northern intensification of the boundary layer, consistent with perturbative analysis. The Munk model, however, displayed more pronounced transient behavior and higher transport, which we attributed to the differences in frictional mechanisms. High non linear regime has also been studied at high Rossby numbers, the flow dynamics approached the Fofonoff solution, characterized by an east-west symmetry and a fully inertial interior.

Overall, our study provides a robust numerical framework for investigating western boundary current intensification and offers valuable insights into the complex interplay of frictional, inertial, and advective processes in ocean dynamics.

Bibliography

1. Vallis, G. K. *Atmospheric and Oceanic Fluid Dynamics: Fundamentals and Large-Scale Circulation* 2nd ed. (Cambridge University Press, 2017).

2. Veronis, G. Wind-driven ocean circulation—Part 1. Linear theory and perturbation analysis. *Deep Sea Research and Oceanographic Abstracts* **13,** 17–29. ISSN: 0011-7471. https://www.sciencedirect.com/science/article/pii/0011747166900039 (1966).

3. Veronis, G. Wind-driven ocean circulation—Part 2. Numerical solutions of the non-linear problem. *Deep Sea Research and Oceanographic Abstracts* **13,** 31–55. ISSN: 0011-7471. https://www.sciencedirect.com/science/article/pii/0011747166900040 (1966).

4. Bryan, K. A Numerical Investigation of a Nonlinear Model of a Wind-Driven Ocean. *Journal of the Atmospheric Sciences* **20,** 594–606. https://api.semanticscholar.org/CorpusID:120974254 (1963).

5. Munk, W. H. ON THE WIND-DRIVEN OCEAN CIRCULATION. *Journal of Atmospheric Sciences* **7,** 80–93. https://journals.ametsoc.org/view/journals/atsc/7/2/1520-0469_1950_007_0080_otwdoc_2_0_co_2.xml (1950).

6. Ierley, G. R. & Young, W. R. Viscous Instabilities in the Western Boundary Layer. *Journal of Physical Oceanography* **21,** 1323–1332. https://journals.ametsoc.org/view/journals/phoc/21/9/1520-0485_1991_021_1323_viitwb_2_0_co_2.xml (1991).

7. Miller, L., Deremble, B. & Venaille, A. Gyre turbulence: Anomalous dissipation in a two-dimensional ocean model. *Phys. Rev. Fluids* **9,** L051801. https://link.aps.org/doi/10.1103/PhysRevFluids.9.L051801 (5 May 2024).

8. *Global Ocean Hourly Sea Surface Wind and Stress from Scatterometer and Model* 2025.